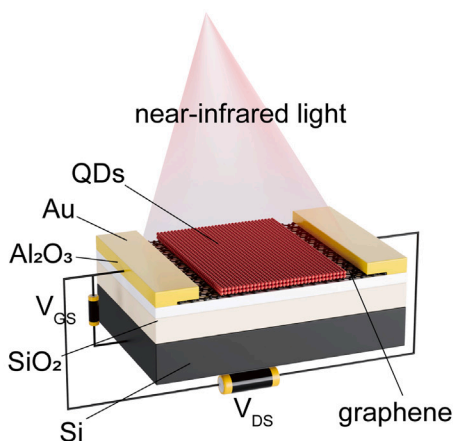


Article

Dielectric engineered graphene transistors for high-performance near-infrared photodetection



- Al_2O_3 mitigates the impact of phonon scattering on graphene.
- The responsivity of the photodetector has been significantly enhanced.
- The preparation process is compatible with CMOS technology.

Weijian Zhou,
Tieying Ma, Ye
Tian, Yixin Jiang,
Xuechao Yu

mty@cjlu.edu.cn (T.M.)
xcyu2022@sinano.ac.cn (X.Y.)

Highlights

The carrier mobility of silicon-based graphene transistors is very low

Dielectric engineering enhances carrier mobility and is CMOS-compatible

The graphene/ Ag_2Te photodetector exhibits high responsivity and detectivity



Article

Dielectric engineered graphene transistors
for high-performance near-infrared photodetectionWeijian Zhou,¹ Tieying Ma,^{1,*} Ye Tian,² Yixin Jiang,¹ and Xuechao Yu^{2,3,*}

SUMMARY

Graphene, known for its ultrahigh carrier mobility and broadband optical absorption, holds significant potential in optoelectronics. However, the carrier mobility of graphene on silicon substrates experienced a marked decrease due to surface roughness, phonon scattering affects. Here we report carrier mobility enhancement of graphene dielectric engineering. Through the fabrication of devices utilizing Si/SiO₂/Al₂O₃/graphene layers and subsequent electrical characterization, our findings illustrate the navigable nature of the Al₂O₃ dielectric layer is navigable for reducing the SiO₂ phonon scattering and increasing graphene's carrier mobility by up to ~8000 cm²V⁻¹s⁻¹. Furthermore, the improvement in carrier mobility of graphene has been utilized in the hybrid near-infrared photodetector, resulting in outstanding responsivity of ~400 AW⁻¹, detectivity of ~2.2 × 10¹¹ Jones in the graphene/Ag₂Te detector. Our study establishes pathways for the seamless integration of graphene or other 2D materials within the standard CMOS processes, thereby facilitating the fabrication of advanced optoelectronic devices.

INTRODUCTION

Charge carrier mobility (μ) stands as a crucial metric for materials destined for electronic devices like field-effect transistors (FETs). It determines the transit time of charge carriers across the device channel. Graphene,^{1–3} a two-dimensional material renowned for its remarkable electrical and mechanical properties, holds great promise in diverse fields, particularly in electronics and optoelectronics. One of the most important properties of graphene is its extremely high charge carrier mobility.⁴ Under ideal conditions, monolayer graphene (SLG) can achieve carrier mobilities of approximately 200,000 cm²V⁻¹s⁻¹ at room temperature.⁵ Numerous factors, including surface roughness,^{6–9} doping,¹⁰ and phonon scattering,^{10–12} limit the intrinsic carrier mobility of graphene.

Ensuring high-quality graphene remains a formidable challenge in graphene applications.^{13,14} The choice of substrate material plays a pivotal role in determining the performance of graphene devices. Silicon dioxide (SiO₂), widely adopted for its cost-effectiveness, robustness, and compatibility with standard CMOS techniques, is a popular choice. However, investigations have shown that transferring SLG onto silicon substrates to form graphene/silicon structures for device production resulted in limited carrier mobility of roughly 3000 cm²V⁻¹s⁻¹,¹⁵ with phonon scattering being a prominent component. Phonon scattering refers to the phenomenon in which electrons in graphene interact with lattice vibrations, leading to energy transfer. Notably, the roughness of the SiO₂ surface introduces surface contaminants and imperfections to the graphene, resulting in significant lattice vibration scatterings. In addition, owing to the low phonon frequencies of SiO₂, there exists a pronounced interaction between graphene and the substrate, consequently resulting in intensified phonon scattering.

Researchers have explored various techniques to mitigate the effects of phonon scattering on the carrier mobility of graphene transistors. For example, the transfer of graphene onto hexagonal boron nitride (h-BN) and its subsequent encapsulation between h-BN layers, creating a sandwich structure known as h-BN/graphene/h-BN,^{5,16} has shown significant promise. These strategies, combined with meticulous atomic-level cleaning¹⁶ of the SiO₂ substrate and protective encapsulation with h-BN,⁵ have yielded impressive room temperature carrier mobilities of $\mu = 70000$ cm²V⁻¹s⁻¹ for single-crystal graphene and $\mu = 10000$ cm²V⁻¹s⁻¹ for polycrystalline graphene.⁵ However, these efforts, while successful in isolated exceptions with diminutive samples, are not compatible with CMOS processes, making it impossible to compete with conventional semiconducting transistors. To address this challenge, we have introduced an innovative approach employing an aluminum oxide (Al₂O₃) dielectric layer to alleviate the impact of phonon scattering induced by SiO₂. By constructing a SiO₂/Al₂O₃/graphene structure, we significantly diminish the adverse effects of SiO₂-induced phonon scattering on the carrier mobility of graphene, leading to marked enhancements in graphene carrier mobility. The hybrid structure of infrared detectors combines the substantial absorption capability of quantum dots with the superior charge carrier mobility of semiconductors, making it a widely employed technology. In recent years, a substantial body of

¹College of Optical and Electronic Technology, China Jiliang University, Hangzhou 310013, China²Key Laboratory of Multifunctional Nanomaterials and Smart Systems, Suzhou Institute of Nano-Tech and Nano-Bionics, Chinese Academy of Sciences, Suzhou, Jiangsu 215123, China³Lead contact^{*}Correspondence: mtj@cjlu.edu.cn (T.M.), xcyu2022@sinano.ac.cn (X.Y.)<https://doi.org/10.1016/j.isci.2024.109314>

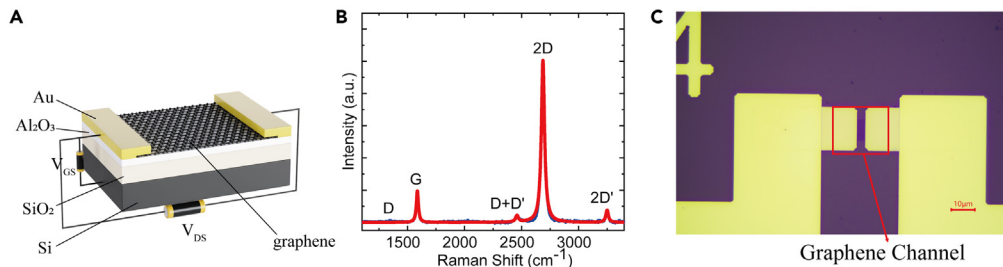


Figure 1. The structure of graphene transistors and material performance characterization

- (A) Structural schematic of Si/SiO₂/Al₂O₃/Graphene.
- (B) Raman spectra of the transferred graphene onto the Al₂O₃ substrate.
- (C) Device image captured through metallographic microscopy.

literature has focused on the integration of graphene into these hybrid structure infrared detectors.^{17–21} This integration has resulted in significant improvements in the performance of photodetectors, particularly in areas such as response time, responsivity, and detectivity.^{22–26} The exceptional properties of hybrid structure detectors are greatly attributed to the application of high-mobility graphene.

RESULTS AND DISCUSSION

Figure 1A elucidates the structural configuration of the prepared graphene transistors in this work. The single-layer graphene (SLG) was synthesized on copper foil the chemical vapor deposition (CVD) technique, and then the graphene was transferred onto the substrate surface of Si/SiO₂ (285 nm)/Al₂O₃ (10 nm).²⁷

The quality of the transferred graphene was evaluated using Raman spectroscopy under 514 nm laser excitation, as presented in Figure 1B. The G peak was observed at approximately 1587 cm⁻¹, while the 2D peak was situated at about 2692 cm⁻¹, boasting a full width at half-maximum(FWHM)(2D) ≈ 32 cm⁻¹ and I(2D)/I(G) ≈ 5.4. Notably, the absence of a discernible D peak in the spectra demonstrated that the structural defects are not introduced into the graphene by the wet transfer procedure.^{28,29}

To assess the quality of the prepared SLG, we conducted the Raman mapping measurements over a scanning area of 25 μm × 25 μm. In Figure 2A, we illustrate the distribution of full width at half-maximum (FWHM) concerning the 2D peak over the entire mapping region, providing a visual representation of graphene quality distribution. Figures 2B–2F show Raman data from mapping: including I(2D)/I(G), A(2D)/A(G), FWHM(G), FWHM(2D), and Pos(2D) as a function of Pos(G). The position of the G peak in graphene is primarily influenced by doping and strain levels. Consequently, the variation in Pos(G) reflects, to some extent, the degree of doping^{30,31} and strain³² in the graphene sample. We obtained these results under the conditions of a 10 nm thick Al₂O₃ dielectric layer, as depicted in Figure 2. In this scenario, the variation in Pos(G) spans from 1583 cm⁻¹ to 1590 cm⁻¹ while the average FWHM(2D) maintains around 32 ± 1 cm⁻¹. Figures 2B–2D illustrates the changes in I(2D)/I(G), A(2D)/A(G), FWHM(G), and FWHM(2D) concerning Pos(G), indicating minimal differences in doping and strain within the SLG layer. The average A(2D)/A(G) value stands at 5.5 ± 0.5. The high A(2D)/A(G) ratio serves as an indicator of intrinsic samples,³¹ particularly when coupled with FWHM(G) ≈ 17 ± 1.5 cm⁻¹, as well as Pos(G) ≈ 1587 cm⁻¹ and Pos(2D) ≈ 2692 cm⁻¹.

Then, we employed CMOS processes to fabricate 25 μm × 25 μm single-layer graphene (SLG) pattern arrays, constructing graphene transistors with different channel lengths, as visually represented in Figure 1C. We performed comprehensive measurements and presented the electrical characteristics of these transistor devices. The transfer characteristics corresponding to SiO₂ substrates with 10 nm thick Al₂O₃ are shown in Figure 3A. In our analysis, we utilized $\mu = \frac{g_m \cdot L_{ch}}{w \cdot V_d \cdot C_{ox}}$ to calculate the carrier mobility of graphene. Here, L_{ch} and w represent the length and width of the graphene channel, V_d signifies the voltage between the source and drain, g_m stands for the transconductance, and C_{ox} corresponds to the capacitance of the dielectric layer. The capacitance C_{ox} can be written by $C_{ox} = \left(\frac{1}{C_{SiO_2}} + \frac{1}{C_{Al_2O_3}} \right)^{-1}$, where C_{SiO_2} and $C_{Al_2O_3}$ denote the capacitance of SiO₂ and the capacitance of Al₂O₃, respectively. The carrier mobility results, as presented in Figure 3B, were obtained through computational analysis. It is evident that the introduction of a 10 nm Al₂O₃ dielectric layer substantially boosts the carrier mobility of graphene when compared to the SiO₂ substrate.

The dielectric constant represents a fundamental property delineating how materials respond to an electric field. It quantifies the relationship between the internal electric field strength and an externally applied electric field. Al₂O₃ possesses a dielectric constant of 8.15, while SiO₂ exhibits a dielectric constant of 3.91. Notably, the equivalent oxide thickness (EOT) plays a significant role in carrier mobility in FETs.^{33–35} EOT influences the distribution of the electric field within the device and a reduced EOT results in a more pronounced electric field effect. Since the carrier mobility is a measure of electron movement speed, a stronger electric field can facilitate higher mobility, leading to increased carrier mobility. The standard method used to calculate EOT is $t_{ox} = \frac{L}{\epsilon_r}$.

While the introduction of the Al₂O₃ dielectric layer in the device has indeed increased the equivalent oxide thickness (EOT) to some extent, it has also significantly enhanced carrier mobility. Al₂O₃, characterized as a high-k dielectric, offers several advantages that positively impacts carrier mobility and is chosen as an example in this work. High-k materials effectively mitigate the effects of externally applied electric fields, facilitating enhanced electron polarization and diminishing the influence of these electric fields. This translates into an augmented electron mobility within the material, thereby yielding an overall enhancement in carrier mobility.

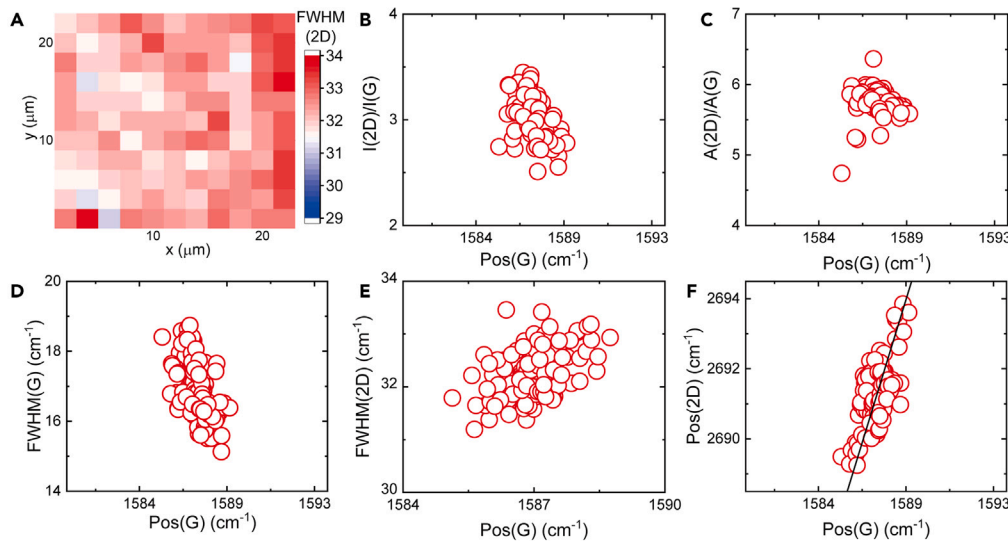


Figure 2. The Raman mapping of the prepared graphene on Si/SiO₂/Al₂O₃ substrate

(A) Image of FWHM of graphene 2D Raman peak with an area of 25 $\mu\text{m} \times 25 \mu\text{m}$ under the conditions of a 10 nm Al₂O₃ dielectric layer to map the distribution of graphene's FWHM. Plots of (B) I(2D)/I(G), (C)A(2D)/A(G), (D)FWHM(G), (E) FWHM(2D), and (F) Position of 2D peak as functions of position of G peak.

Figure 3C illustrates the influence of varying channel lengths on carrier mobility. Notably, the device featuring a 10 nm thick Al₂O₃ layer achieves a remarkable peak in carrier mobility, reaching an impressive $8000 \text{ cm}^2 \text{V}^{-1} \text{s}^{-1}$, as depicted in the figures. This substantial enhancement is a significant leap from the mobility of approximately $3000 \text{ cm}^2 \text{V}^{-1} \text{s}^{-1}$ observed on SiO₂ alone. However, as the Al₂O₃ thickness approaches 20 nm, the device's carrier mobility diminishes to roughly $6000 \text{ cm}^2 \text{V}^{-1} \text{s}^{-1}$, as presented in Figure 3D. This intriguing pattern suggests that augmenting the Al₂O₃ thickness may not yield indefinite improvements in device mobility. At a specific thickness, it becomes evident that the combined effects of the Al₂O₃ interface and electric field significantly amplify carrier mobility. This provides essential insight into the intricate correlation between material thickness and carrier transport mechanisms within these devices.

To investigate the influence of carrier mobility on photodetector performance, we fabricated a graphene/Ag₂Te photodetector by using Ag₂Te quantum dots as the light-absorbing layer.^{36–38} The fabrication details can be found in the supporting information. The electrical characteristics of the device were recorded in the dark and under 1064 nm laser illumination, as shown in Figure 4B. The I_d-V_d curves exhibited linear and symmetric characteristics, indicating ohmic contacts in the device. By comparing the performance at different Al₂O₃ thicknesses, we observed an improvement in responsivity (*R*) under high carrier mobility conditions. The responsivity reached approximately 400 AW^{-1} for the graphene/Ag₂Te photodetector (Figure 4C). For graphene photodetectors, the specific detectivity (*D**) of the device is influenced by the noise current.^{39,40} To address this issue, we conducted noise spectrum measurements separately for the SiO₂ substrate and the SiO₂ substrate with 10 nm Al₂O₃ (Figure 4A). With the addition of Al₂O₃, the transistors exhibited a lower noise density spectrum (SID). We postulate that this could be attributed to the improved interface quality of Al₂O₃ compared to SiO₂. Reduced phonon scattering between graphene and Al₂O₃, compared to SiO₂, is likely to lower transistor noise, elucidating the reasons behind the enhanced device carrier mobility. Increased carrier mobility equates to higher carrier transport efficiency, resulting in an enhanced rate of transport for photogenerated carriers across the graphene. This, in turn, leads to a faster response time for the detector. Our experimental findings indicate that the addition of a 10 nm Al₂O₃ substrate improves the response time from 1.75 s to 1.52 s when compared to a graphene/Ag₂Te detector with a SiO₂ substrate (Figure 4D). In comparison with the test data of Ag₂Te in ref. 38, at a wavelength of 1064 nm, the *R* in the literature is approximately 0.1 AW^{-1} , which is comparable to our data without Al₂O₃. It is clearly demonstrated that the addition of the Al₂O₃ dielectric layer significantly contributes to enhancing the detector's performance.

Conclusions

To enhance graphene carrier mobility, we propose an innovative approach by integrating an Al₂O₃ dielectric layer into the conventional Si/SiO₂/graphene structure. Compared to the traditional method of transferring graphene onto SiO₂, our approach achieves carrier mobilities of approximately $8000 \text{ cm}^2 \text{V}^{-1} \text{s}^{-1}$. As per our experimental results, the optimal Al₂O₃ thickness is approximately 10 nm. Beyond this thickness, the boosting effect of Al₂O₃ on carrier mobility reduces. With the enhanced mobility, we achieve responsivity(*R*) up to $\sim 400 \text{ AW}^{-1}$, and the detectivity(*D**) increased to $\sim 2.2 \times 10^{11} \text{ Jones}$. Consequently, the response time of the device is slightly improved. By integrating Al₂O₃, a material compatible with CMOS processes and large-area fabrication procedures, we achieve substantial enhancements in mobility, thus reducing the dependence on h-BN encapsulation. Our strategy can also be implemented by various nanoelectronics, or optoelectronics, where the capabilities of CMOS and advancements in carrier mobility play a pivotal role.

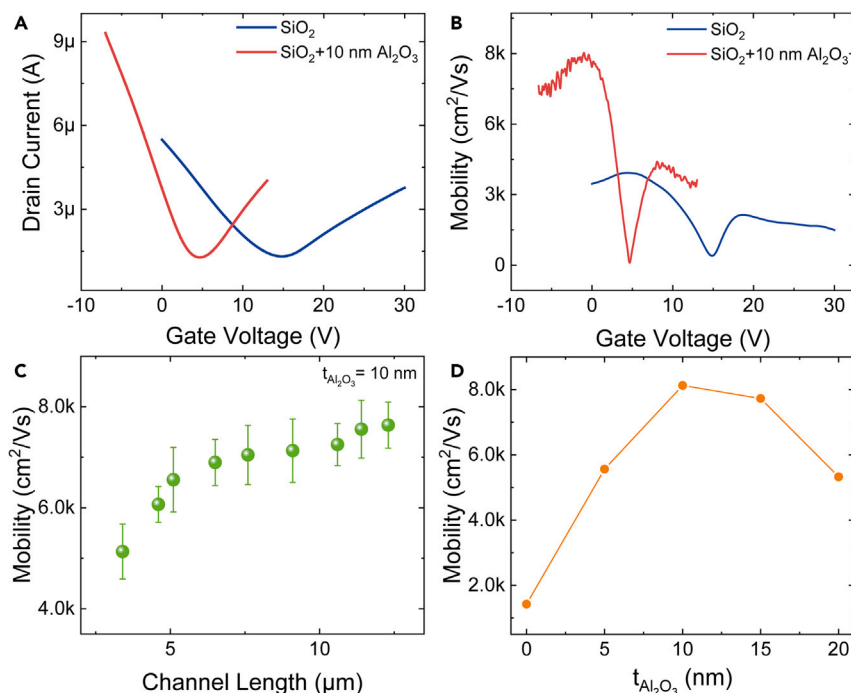


Figure 3. Electrical characteristics of graphene transistors

The bias voltage is 10 mV, the channel length is 12.5 μm in (A), (B), (C) and (D).

(A) Transfer characteristics on SiO_2 substrate and $\text{SiO}_2 + 10 \text{ nm Al}_2\text{O}_3$ substrates.

(B) Correlation with mobility as a function of gate voltage on SiO_2 substrate and $\text{SiO}_2 + 10 \text{ nm Al}_2\text{O}_3$ substrate.

(C) Error plots depicting carrier mobility calculated for varying graphene channel lengths on Al_2O_3 dielectric layers deposited on silicon dioxide substrates with thicknesses of 10 nm.

(D) The correlation between the carrier mobility of graphene and the thickness of Al_2O_3 .

Summary of supplementary information

Supplementary information is available for this publication which includes; S1 and S2: Raman mapping of graphene transferred onto Al_2O_3 substrates of various thicknesses. S3: The thickness gradient results of Al_2O_3 dielectric layers obtained by AFM measurements. S4: Surface AFM characterization images of Al_2O_3 dielectric layers with different thicknesses. S5: Noise spectra of graphene and graphene/ Ag_2Te photodetector. S6: Carrier mobility for varying graphene channel lengths. S7: Time-dependent photocurrent measurements under near-infrared laser illumination with wavelength ranging from 808 nm to 1550 nm S8: Laser power density-dependent photocurrent measurements of graphene/ Ag_2Te photodetectors with different thicknesses of Al_2O_3 .

Limitations of the study

In this study, Al_2O_3 was employed as the dielectric layer for experimental validation. While other high-k dielectrics exhibit similar properties, their effectiveness remains theoretically inferred without experimental verification.

STAR★METHODS

Detailed methods are provided in the online version of this paper and include the following:

- [KEY RESOURCES TABLE](#)
- [RESOURCE AVAILABILITY](#)
 - Lead contact
 - Materials availability
 - Data and code availability
- [EXPERIMENTAL MODEL AND STUDY PARTICIPANT DETAILS](#)
- [METHOD DETAILS](#)
 - Device fabrication
 - Performance characterization
- [QUANTIFICATION AND STATISTICAL ANALYSIS](#)

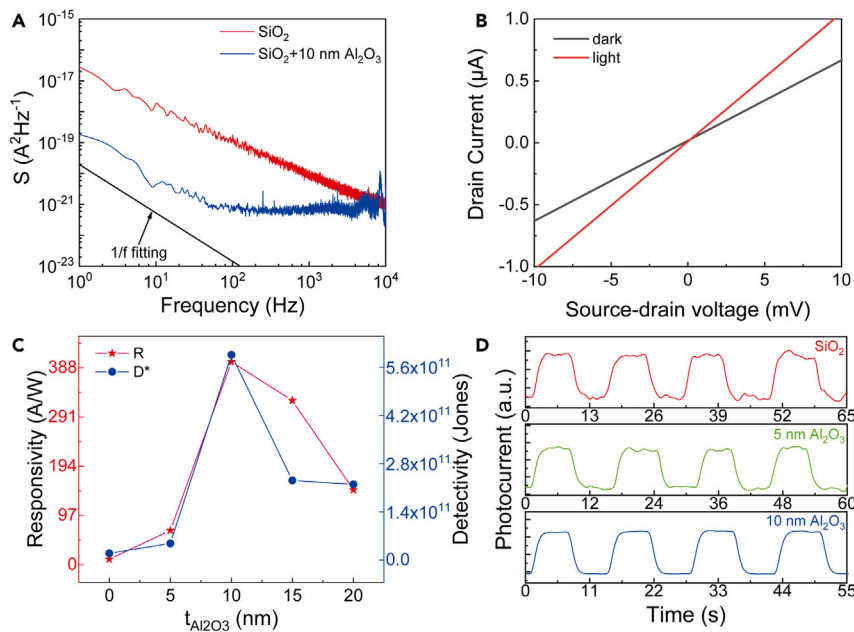


Figure 4. Performance of the graphene/Ag₂Te photodetector

(A) Noise spectra of graphene and graphene/Ag₂Te photodetector as a function of frequency measured at a constant bias voltage of 10 mV.

(B) I_d - V_d curves of the graphene/Ag₂Te photodetector measured in dark and under laser illumination ($\lambda: 1064 \text{ nm}$; power: 1.72 mWcm^{-2}).

(C) Responsivity and detectivity of the graphene/Ag₂Te photodetector measured at wavelength 1064 nm and power density 1.72 mWcm^{-2} .

(D) Temporal response of the device to pulsed light of 1064 nm.

SUPPLEMENTAL INFORMATION

Supplemental information can be found online at <https://doi.org/10.1016/j.isci.2024.109314>.

ACKNOWLEDGMENTS

This work was financially supported by the National Natural Science Foundation of China (no. 62375279) and the Suzhou Industrial Science and Technology Program (SYG202340). The authors are grateful for the technical support from the Nano-X from Suzhou Institute of Nano-Tech and Nano-Bionics, Chinese Academy of Sciences (SINANO). The results are characterized by the Photocurrent System (Tuo Tuo Technology).

AUTHOR CONTRIBUTIONS

The ideas and supervision for this article were contributed by X.Y. and T.M. W.Z., Y.T., and Y.J. actively participated in the device fabrication, optoelectronic testing, analysis, and the writing and revision of the manuscript. All the authors participated in writing and revising the manuscript.

DECLARATION OF INTERESTS

The authors declare no conflicts of interest.

Received: November 15, 2023

Revised: January 5, 2024

Accepted: February 17, 2024

Published: February 23, 2024

REFERENCES

- Kim, K.S., Zhao, Y., Jang, H., Lee, S.Y., Kim, J.M., Kim, K.S., Ahn, J.-H., Kim, P., Choi, J.-Y., and Hong, B.H. (2009). Large-scale pattern growth of graphene films for stretchable transparent electrodes. *Nature* 457, 706–710.
- Novoselov, K.S., Geim, A.K., Morozov, S.V., Jiang, D., Katsnelson, M.I., Grigorieva, I.V., Dubonos, S.V., and Firsov, A.A. (2005). Two-dimensional gas of massless Dirac fermions in graphene. *Nature* 438, 197–200.
- Zhang, Y., Tan, Y.-W., Stormer, H.L., and Kim, P. (2005). Experimental observation of the quantum Hall effect and Berry's phase in graphene. *Nature* 438, 201–204.
- Geim, A.K., and Novoselov, K.S. (2007). The rise of graphene. *Nat. Mater.* 6, 183–191.
- De Fazio, D., Purdie, D.G., Ott, A.K., Braeuninger-Weimer, P., Khodkov, T., Goossens, S., Taniguchi, T., Watanabe, K., Liveri, P., Koppens, F.H.L., et al. (2019). High-Mobility, Wet-Transferred Graphene Grown

- by Chemical Vapor Deposition. *ACS Nano* 13, 8926–8935.
6. Ishigami, M., Chen, J.H., Cullen, W.G., Fuhrer, M.S., and Williams, E.D. (2007). Atomic Structure of Graphene on SiO₂. *Nano Lett.* 7, 1643–1648.
 7. Katsnelson, M.I., and Geim, A.K. (2008). Electron scattering on microscopic corrugations in graphene. *Phil. Trans. R. Soc. A* 366, 195–204.
 8. Morozov, S.V., Novoselov, K.S., Katsnelson, M.I., Schedin, F., Elias, D.C., Jaszczak, J.A., and Geim, A.K. (2008). Giant intrinsic carrier mobilities in graphene and its bilayer. *Phys. Rev. Lett.* 100, 016602.
 9. Wang, Q., Li, Y., Bai, B., Mao, W., Wang, Z., and Ren, N. (2014). Effects of silicon dioxide surface roughness on Raman characteristics and mechanical properties of graphene. *RSC Adv.* 4, 55087–55093.
 10. Chen, J.H., Jang, C., Adam, S., Fuhrer, M.S., Williams, E.D., and Ishigami, M. (2008). Charged-impurity scattering in graphene. *Nat. Phys.* 4, 377–381.
 11. Adam, S., Hwang, E.H., Galitski, V.M., and Das Sarma, S. (2007). A self-consistent theory for graphene transport. *Proc. Natl. Acad. Sci. USA* 104, 18392–18397.
 12. Chen, J.-H., Jang, C., Xiao, S., Ishigami, M., and Fuhrer, M.S. (2008). Intrinsic and extrinsic performance limits of graphene devices on SiO₂. *Nat. Nanotechnol.* 3, 206–209.
 13. Chakraborty, S.K., Kundu, B., Nayak, B., Dash, S.P., and Sahoo, P.K. (2022). Challenges and opportunities in 2D heterostructures for electronic and optoelectronic devices. *iScience* 25, 103942.
 14. Zhang, Q., Liu, C., and Zhou, P. (2023). 2D materials readiness for the transistor performance breakthrough. *iScience* 26, 106673.
 15. Li, X., Zhu, Y., Cai, W., Borysiak, M., Han, B., Chen, D., Piner, R.D., Colombo, L., and Ruoff, R.S. (2009). Transfer of large-area graphene films for high-performance transparent conductive electrodes. *Nano Lett.* 9, 4359–4363.
 16. Purdie, D.G., Pugno, N.M., Taniguchi, T., Watanabe, K., Ferrari, A.C., and Lombardo, A. (2018). Cleaning interfaces in layered materials heterostructures. *Nat. Commun.* 9, 5387.
 17. Gorecki, J., and Krause, S. (2024). Numerical investigation of a graphene-on-semiconductor device for optical monitoring of cell electrophysiology. *iScience* 27, 108554.
 18. Guo, H., and Qi, W. (2022). New materials and designs for 2D-based infrared photodetectors. *Nano Res.* 16, 3074–3103.
 19. Liu, T., Tong, L., Huang, X., and Ye, L. (2019). Room-temperature infrared photodetectors with hybrid structure based on two-dimensional materials. *Chin. Phys. B* 28, 017302.
 20. Wang, F., Zhang, Y., Gao, Y., Luo, P., Su, J., Han, W., Liu, K., Li, H., and Zhai, T. (2019). 2D Metal Chalcogenides for IR Photodetection. *Small* 15, e1901347.
 21. Yu, X., Yu, P., Wu, D., Singh, B., Zeng, Q., Lin, H., Zhou, W., Lin, J., Suenaga, K., Liu, Z., and Wang, Q.J. (2018). Atomically thin noble metal dichalcogenide: a broadband mid-infrared semiconductor. *Nat. Commun.* 9, 1545.
 22. Antosiewicz, T.J., Wadell, C., and Langhammer, C. (2015). Plasmon-Assisted Indirect Light Absorption Engineering in Small Transition Metal Catalyst Nanoparticles. *Adv. Opt. Mater.* 3, 1591–1599.
 23. Li, A., Chen, Q., Wang, P., Gan, Y., Qi, T., Wang, P., Tang, F., Wu, J.Z., Chen, R., Zhang, L., and Gong, Y. (2019). Ultrahigh-Sensitive Broadband Photodetectors Based on Dielectric Shielded MoTe₂/Graphene/SnS₂ p-g-n Junctions. *Adv. Mater.* 31, e1805656.
 24. Long, M., Liu, E., Wang, P., Gao, A., Xia, H., Luo, W., Wang, B., Zeng, J., Fu, Y., Xu, K., et al. (2016). Broadband Photovoltaic Detectors Based on an Atomically Thin Heterostructure. *Nano Lett.* 16, 2254–2259.
 25. Yu, W., Li, S., Zhang, Y., Ma, W., Sun, T., Yuan, J., Fu, K., and Bao, Q. (2017). Near-Infrared Photodetectors Based on MoTe₂/Graphene Heterostructure with High Responsivity and Flexibility. *Small* 13, 1700268.
 26. Zhang, K., Fang, X., Wang, Y., Wan, Y., Song, Q., Zhai, W., Li, Y., Ran, G., Ye, Y., and Dai, L. (2017). Ultrasensitive Near-Infrared Photodetectors Based on a Graphene-MoTe₂-Graphene Vertical van der Waals Heterostructure. *ACS Appl. Mater. Interfaces* 9, 5392–5398.
 27. Suk, J.W., Kitt, A., Magnuson, C.W., Hao, Y., Ahmed, S., An, J., Swan, A.K., Goldberg, B.B., and Ruoff, R.S. (2011). Transfer of CVD-grown monolayer graphene onto arbitrary substrates. *ACS Nano* 5, 6916–6924.
 28. Faugeras, C., Faugeras, B., Orlita, M., Potemski, M., Nair, R.R., and Geim, A.K. (2010). Thermal conductivity of graphene in corbino membrane geometry. *ACS Nano* 4, 1889–1899.
 29. Ferrari, A.C., Meyer, J.C., Scardaci, V., Casiraghi, C., Lazzeri, M., Mauri, F., Piscanec, S., Jiang, D., Novoselov, K.S., Roth, S., and Geim, A.K. (2006). Raman spectrum of graphene and graphene layers. *Phys. Rev. Lett.* 97, 187401.
 30. Basko, D.M., Piscanec, S., and Ferrari, A.C. (2009). Electron-electron interactions and doping dependence of the two-phonon Raman intensity in graphene. *Phys. Rev. B* 80, 165413.
 31. Das, A., Pisana, S., Chakraborty, B., Piscanec, S., Saha, S.K., Waghmare, U.V., Novoselov, K.S., Krishnamurthy, H.R., Geim, A.K., Ferrari, A.C., and Sood, A.K. (2008). Monitoring dopants by Raman scattering in an electrochemically top-gated graphene transistor. *Nat. Nanotechnol.* 3, 210–215.
 32. Mohiuddin, T.M.G., Lombardo, A., Nair, R.R., Bonetti, A., Savini, G., Jalil, R., Bonini, N., Basko, D.M., Galotis, C., Marzari, N., et al. (2009). Uniaxial strain in graphene by Raman spectroscopy: Peak splitting, Grüneisen parameters, and sample orientation. *Phys. Rev. B* 79, 205433.
 33. Appenzeller, J., Knob, J., Derycke, V., Martel, R., Wind, S., and Avouris, P. (2002). Field-modulated carrier transport in carbon nanotube transistors. *Phys. Rev. Lett.* 89, 126801.
 34. Xiao, M., Qiu, C., Zhang, Z., and Peng, L.M. (2017). Atomic-Layer-Deposition Growth of an Ultrathin HfO₂ Film on Graphene. *ACS Appl. Mater. Interfaces* 9, 34050–34056.
 35. Yee-Chia, Y., Tsu-Jae, K., and Chenming, H. (2003). MOSFET gate leakage modeling and selection guide for alternative gate dielectrics based on leakage considerations. *IEEE Trans. Electron Devices* 50, 1027–1035.
 36. Liu, Z.Y., Liu, A.A., Fu, H., Cheng, Q.Y., Zhang, M.Y., Pan, M.M., Liu, L.P., Luo, M.Y., Tang, B., Zhao, W., et al. (2021). Breaking through the Size Control Dilemma of Silver Chalcogenide Quantum Dots via Trialkylphosphine-Induced Ripening: Leading to Ag₂Te Emitting from 950 to 2100 nm. *J. Am. Chem. Soc.* 143, 12867–12877.
 37. Ouyang, J., Graddage, N., Lu, J., Zhong, Y., Chu, T.-Y., Zhang, Y., Wu, X., Kodra, O., Li, Z., Tao, Y., and Ding, J. (2021). Ag₂Te Colloidal Quantum Dots for Near-Infrared-II Photodetectors. *ACS Appl. Nano Mater.* 4, 13587–13601.
 38. Peng, L., Wang, Y., Ren, Y., Wang, Z., Cao, P., and Konstantatos, G. (2024). InSb/InP core-shell colloidal quantum dots for sensitive and fast short-wave infrared photodetectors. *ACS Nano* 18, 5113–5121.
 39. Wang, F., Zhang, T., Xie, R., Wang, Z., and Hu, W. (2023). How to characterize figures of merit of two-dimensional photodetectors. *Nat. Commun.* 14, 2224.
 40. Yu, X., Li, Y., Hu, X., Zhang, D., Tao, Y., Liu, Z., He, Y., Haque, M.A., Liu, Z., Wu, T., and Wang, Q.J. (2018). Narrow bandgap oxide nanoparticles coupled with graphene for high performance mid-infrared photodetection. *Nat. Commun.* 9, 4299.
 41. Wind, S.J., Appenzeller, J., Martel, R., Derycke, V., and Avouris, P. (2002). Vertical scaling of carbon nanotube field-effect transistors using top gate electrodes. *Appl. Phys. Lett.* 80, 3817–3819.
 42. Gahoi, A., Kataria, S., Driussi, F., Venica, S., Pandey, H., Esseni, D., Selmi, L., and Lemme, M.C. (2020). Dependable Contact Related Parameter Extraction in Graphene-Metal Junctions. *Adv. Electron.* 6, 2000386.

STAR★METHODS

KEY RESOURCES TABLE

REAGENT or RESOURCE	SOURCE	IDENTIFIER
<u>Software and algorithms</u>		
Origin 2018	Origin Lab	www.originlab.com
Adobe Illustrator	Adobe	www.adobe.com

RESOURCE AVAILABILITY

Lead contact

Additional inquiries and requests for resources and reagents should be directed to and will be fulfilled by the lead contact, X. Y. (xcyu2022@sinano.ac.cn).

Materials availability

The work presented in this paper did not produce any new materials.

Data and code availability

All the data in the manuscript were analyzed using Origin 2018.

Any additional information necessary for reanalyzing the data presented in this paper is accessible from the [lead contact](#) upon request.

EXPERIMENTAL MODEL AND STUDY PARTICIPANT DETAILS

This study did not involve any experimental models or study participants.

METHOD DETAILS

Device fabrication

To produce Al₂O₃ films on Si/SiO₂ substrates, we employed Atomic Layer Deposition (ALD),^{35,41} allowing for precise control of film thickness. The resulting substrates underwent a meticulous cleaning process involving acetone and isopropanol ultrasonication to ensure pristine conditions for transferring Single-Layer Graphene (SLG). Subsequently, after confirming the quality of the transferred SLG through Raman spectroscopy, we proceeded with the fabrication of the devices. Using MA6 equipment, we performed ultraviolet photolithography and plasma etching to define the appropriate structures for the Transmission Line Method (TLM).⁴² Finally, we deposited Ti/Au metal electrodes with thicknesses of 10/100 nm through electron beam evaporation, culminating in the construction of the Field-Effect Transistor (FET) structure.

Performance characterization

We conducted Raman measurements using a Raman spectrometer equipped with 514 nm laser excitation. Electrical characterizations were examined using a Keithley 2400 and a Keysight B1500A. In a brief description, the emission wavelength of the laser in the near-infrared is controlled by the laser controller and is modulated by the mechanical optical chopper, and then the laser emission is focused on the sample area by an optical lens. The electrical signal is collected by a semiconductor measurement system (Keysight B1500A) and analyzed by a lock-in amplifier (SR830). It is essential to note that all measurements were conducted under ambient conditions at room temperature, and no device encapsulation was applied. Noise spectra are acquired by a low-frequency noise test system consisting of DLPCA-200 (Variable Gain Low Noise Current Amplifier) and DDPCA-300 (Variable Gain Sub-Femtoampere Current Amplifier) with bias supplied by DLPCA-200 at ambient conditions.

QUANTIFICATION AND STATISTICAL ANALYSIS

All data in this paper are processed and presented in Origin 2018. For the calculation and analysis of carrier mobility and photocurrent at different Al₂O₃ thicknesses, error bars were used to represent data from multiple measurements. The averages of each group are connected by line plots, as shown in [Figures 3A, S6](#), and [S8](#).